Energy transfer, structural and luminescent properties of the color tunable phosphor $Y_2WO_6:Sm^{3+}$

D. Espinoza[1], N.L. Allan[2], R. Castillo[1], S. Conejeros[1]*, I. Brito[3], I.R. Martin[4], P. Alemany[5], and J. Llanos[1]*

[1]Departamento de Química, Universidad Católica del Norte, Avda. Angamos 0610, Antofagasta, Chile

[2]School of Chemistry, University of Bristol, Bristol BS8 1TS, United Kingdom

[3]Departamento de Química, Universidad de Antofagasta, Campus Coloso, Antofagasta, Chile

[4] Departamento de Física, Instituto de Materiales y Nanotecnología (IMN), Universidad de La Laguna, Apartado 456, San Cristóbal, S/C de Tenerife, Spain

[5] Departament de Ciència dels Materials i Química Física and Institut de Química Teòrica i Computacional (IQTCUB), Universitat de Barcelona, Diagonal 647, 08028 Barcelona, Spain

Abstract

Inorganic phosphors based on monoclinic Y_2WO_6 doped with Sm^{3+} ions were prepared via conventional solid-state reactions at high temperature. A total of six samples were obtained with different Sm^{3+} concentrations (0–9%). The purity of the as-prepared phases was checked by powder X-ray diffraction (PXRD). The excitation, emission, and time-resolved emission spectra were examined in detail. The experimental decay curves were fitted to the Inokuti–Hirayama model, showing that the Sm^{3+} ions form clusters at all compositions.

Periodic hybrid density functional theory calculations were also carried out on the undoped material and on 144-atom supercells of stoichiometry $Y_{1.9375}Sm_{0.0625}WO_6$ and $Y_{1.875}Sm_{0.125}WO_6$. The different coordination environments at the Y1, Y2 and Y3 sites are analysed in detail. The calculated structure and band gap of Y_2WO_6 are in good agreement with experiment with one potentially important discrepancy in a Y3-O bond length. The thermodynamically favoured substitution sites for Sm, Y2 and Y3, in the supercell are not those observed under the preparation conditions used here, since the experimental Rietveld analysis suggests occupation of Y1 at all concentrations. Analogous calculations for the Eu-doped system highlight marked differences between Eu and Sm despite their similar ionic sizes. The calculated densities of states show the position of the 4f levels in the band gap depend on the

sites occupied by the dopants and thus expect marked differences in the luminescence spectra, opening up possibilities for tuning device performance.

Keywords: Inorganic materials, Solid state reaction, Computer simulations, Luminescence, Optical properties, X-ray diffraction

1. Introduction

Lanthanide ions activated phosphors are characterized by their excellent optical properties. This type of compound has drawn much attention because of potential applications in many fields, such a as solid-state lighting devices, biomedical imaging, plasma display panels, optical sensors, and more recently in solar cells and nano- and biotechnology [1-6]. One of the most investigated rare-earth cations is the trivalent europium ion (Eu^{3+}) due to its characteristic orange-red emission upon irradiation with UV light, corresponding to the $^5D_0 \rightarrow {}^7F_J$ (J=0,4) transition [7-10]. The $^5D_0 \rightarrow {}^7F_1$ transition is a magnetic dipole (MD) transition and the resulting orange emission is largely independent of the chemical environment of the Eu^{3+} dopant. In contrast, the transition $^5D_0 \rightarrow {}^7F_2$ is an electric dipole (ED) transition, and its presence and intensity is greatly influenced by the local symmetry of the Eu^{3+} ion, producing a red emission. Because of the high cost of europium compounds, new orange-red emitters need to be explored. Sm^{3+} is a good competitive candidate as an activator ion in inorganic phosphors. The multicolor luminescent properties of Sm^{3+}-doped phosphors have great potential for use in solid-state lighting devices [11].

The characteristic emission of Sm^{3+} is due to $^4G_{5/2} \rightarrow {}^6H_J$ (J=5/2, 7/2, 9/2, 11/2) transitions. The transitions $^4G_{5/2} \rightarrow {}^6H_{5/2}$ (yellow emission), and $^4G_{5/2} \rightarrow {}^6H_{7/2}$ (orange emission) are magnetic dipole transition (MD), whereas the $^4G_{5/2} \rightarrow {}^6H_{9/2}$ (red emission) transition is an electric dipole transition (ED) [12].

In the present communication we report the synthesis and characterization of new $Y_2WO_6:Sm^{3+}$ inorganic phosphors. Y_2WO_6 was chosen as the host matrix due to its optical activity, and in particular, its ability to compensate for the low absorption coefficient of the Sm^{3+} cation. The great capability of Y_2WO_6 for self-activation, followed by efficient energy transfer to the rare-earth activator, and its high quantum

yield makes this tungstate a very good choice as a host structure for the Sm^{3+}-doped phosphors [13-16]. Put another way, the quantum-yield of yttrium tungstate can be increased by doping with an appropriate amount of Sm^{3+}.

We report the synthesis of $Y_{2-x}Sm_xWO_6$ phosphors via solid-state reaction at high temperature and their photoluminescent features. We carry out an analysis of the energy transfer process between the luminescent excited states of the Sm^{3+} ions and the possible interactions between the activator and the host-matrix. A Rietveld analysis is also carried out in order to determine where the rare–earth cations replace Y^{3+} in the host-structure. Hybrid density functional theory calculations are also carried out to analyse the electronic properties of the doped material, the energetics of Sm-Sm pair interactions leading to dopant clustering and to compare Sm-doping with the results for Eu-doping which have been reported previously [17].

2. Experimental

2.1 Synthesis

All manipulations were performed under ambient conditions, and the starting materials were used as received. $Y_{2-x}Sm_xWO_6$ ($0 \leq x \leq 0.18$) samples were prepared by solid-state reactions at high temperature. Stoichiometric amounts of the precursors, Y_2O_3 (Sigma-Aldrich 99%), Sm_2O_3 (Sigma-Aldrich 99%) and WO_3 (Sigma-Aldrich 99%) were ground in an agate mortar for several minutes. The resulting homogeneous mixtures were then placed in combustion boats (Coors, high alumina) and heated at 973 K for 10 hours. After cooling down to room temperature, the samples were removed and ground into a powder, placed again in the combustion boats, and heated at 1273 K for 10 hours. The procedure was repeated, and the samples were finally heated at 1373 K for another 10 hours.

2.2 Characterization

Powder X-Ray Diffraction (PXRD) data were collected using a Bruker D8 Advance diffractometer fitted with a graphite monochromator. The measured range was $10° \leq 2\theta \leq 60°$, using Cu Kα radiation ($\lambda = 1.54057$ Å) generated at 40 kV and 30 mA. A

full-profile Rietveld analysis of the obtained diffractograms was performed with the Jana2006 software [18]. Diffuse reflectance spectra were recorded with a UV-V-NIR spectrophotometer (VARIANT CARY 5000) and the optical bandgaps were estimated by the Tauc method [19]. Luminescence measurements: excitation spectra were recorded using a JASCO FP-6500 spectrofluorometer with a 150 W xenon lamp as the excitation source. Emission spectra were obtained by exciting the samples at 300 nm using a 400 W Oriel xenon lamp. The spectra were recorded with a system of two convex lenses that collimated and focalized the sample's emission into an optical fiber coupled to a 0.3 m single grating spectrometer (Andor Shamrock-3031-B). The final measurement was carried out using a cooled CCD detector (Newton DU920 N) with a resolution of 0.7 nm and an integration time of 2s. For the lifetime measurements, a tunable optical parameter oscillator (OPO) was used as the excitation source (10 Hz repetition rate, 8ns pulse temporal width) and the time resolved emission was focused on the entrance slit of a monochromator (Triax 180) coupled with a photomultiplier (Hamamatsu r928). The signal was acquired and averaged by an oscilloscope (Lecroy Wavesurfer 424). All measurements were carried out at room temperature.

2.3 Electronic Structure

Periodic ab initio calculations were performed using the CRYSTAL17 code [20-22] to evaluate the relative energies of different possible substitution patterns of Sm in the Y_2WO_6 matrix and the associated electronic structure. Energies were calculated using density functional theory (DFT), adopting the PBE , PBEsol and hybrid HSE06 functionals [23-25]. The atomic Gaussian basis sets used were a 6-311G* basis set for O [26], and effective core pseudopotentials (ECP) with valence basis sets for Y, W and Sm [27-29]. For the calculation of the Coulomb and exchange integrals, tolerance factors of 7, 7, 7, 7, and 14 were used. The convergence criterion for the electronic energy was set at 10^{-7} a.u. [30]. The reciprocal space integration used a mesh of 8×8×8 and 2x2x2 *k*-points in the irreducible Brillouin zone chosen according to the Monkhorst-Pack scheme [31] for primitive cell and supercell calculations, respectively; convergence of the energy with grid size was checked. Full geometry optimisation of the undoped system gave the same structure as an optimisation in

which the space group (*P*2/*c*) was kept fixed. All symmetry constraints were removed in calculations on the doped systems. All supercell calculations were spin-polarized in order to take into account the five (S=5/2) and six (S=3) unpaired f electrons in the Sm^{3+} and Eu^{3+} cations respectively.

2.4 Structural analysis

In rare earth doped phosphors the geometry of the coordination environment of the activator ions is a key factor determining the optical properties and we describe this using continuous shape measures (CShM) [32, 33]. These provide a quantitative measure of the degree of distortion of the coordination sphere around a given atom with respect to the shape of a predefined ideal polyhedron. The CShM for an N-vertex polyhedron *Q* with respect to an ideal polyhedron *P* with the same number of vertices, $S_P(Q)$ is obtained by superimposing the two polyhedra in such a way that the sum of squared distances between their vertices is minimized [33, 34]:

$$S_P(Q) = min\frac{\sum_{i=1}^{N}|\boldsymbol{q}_k-\boldsymbol{p}_k|^2}{\sum_{i=1}^{N}|\boldsymbol{q}_k-\boldsymbol{q}_0|^2}\cdot 100 \qquad (1)$$

where $\mathbf{q}_k$ and $\mathbf{p}_k$ are the coordinates of the vertices of *Q* and *P*, respectively, and $\mathbf{q}_0$ the geometric centre of *Q*. The value of $S_P(Q)$ is found by searching for the translation, rotation, relative size, and vertex pairings that minimize the sum of squared distances between the vertices of *P* and *Q*.

If the two structures have exactly the same shape (but not necessarily the same size) then $S_P(Q) = 0$. Since $S_P(Q)$ is always positive, the larger the value of $S_P(Q)$, the less similar is *Q* to the ideal shape *P*. The maximum value of $S_P(Q)$ is 100, corresponding to the unphysical situation where all vertices of *Q* collapse into a single point [34]. Values severely distorted chemical structures never exceed 50. The main purpose of using CShMs is to characterize the shape of complex coordination geometries with just a few parameters [35-39] and for this we take a reference shape, for instance a perfect cube, and calculate the corresponding shape measure *S(CU-8)* for the distorted structures found experimentally. As a rule of thumb, CShM values below 0.1 are unimportant from a crystallochemical point of view, while those above 3 point towards significant distortions from the reference geometries. Further characterization of the distorted structure is possible by evaluating several CSMs for the same

structure. Since, irrespective of the reference shape and the number of vertices, all CShM values are on the same scale, they can be compared to obtain the best description for the shape and symmetry in each individual case. It is possible also to take the experimental structure as a reference and use the corresponding $S_{exp}(Q_{calc})$ value to check the similarity of a calculated structure with the experimental one.

3. Results and discussion

3.1 X-ray diffraction

The synthesized products were obtained in the form of homogeneous white powders. The measured PXRD profiles indicate that the obtained phase is the monoclinic (*P2/c*) polymorph (ICSD no. 20955) for all $Y_{2-x}Sm_xWO_6$ ($0 \leq x \leq 0.18$) samples, with no peaks from any other phase. Moreover, a systematic shift of the peak positions is seen as the amount of Sm^{3+} increases, indicating that the dopant ion is incorporated into the host matrix, substituting for Y^{3+}. The monoclinic crystal structure of Y_2WO_6 (Figure 1) contains three symmetry-independent yttrium atoms. In the literature [40] Y1(2e) and Y2(2f) have been describes as eightfold coordinate, whereas Y3(4g) is sevenfold coordinate, in all three cases with average Y-O distances in the range 2.3-2.4 Å. A closer look at the coordination environment around the Y3(4g) atoms in the reported experimental structure shows, however, that there is an additional O atom at a relatively close distance of 3.138 Å. This is much shorter than the distances to the second coordination shell of any of the three sites; the closest second neighbour O atoms are found at 4.061 Å, 3.872 Å, and 3.775 Å from Y1, Y2, and Y3, respectively. For this reason we think that the Y3 sites are better described by a 7+1 coordination than being simply sevenfold coordinated. As shown later, the additional O atom around the Y3 cations plays an interesting role when Y3 is replaced by Ln^{3+}cations such as Eu^{3+} or Sm^{3+}, which are larger than Y^{3+} [41]. The 8-fold coordinate ionic radii of Sm^{3+}, Eu^{3+} and Y^{3+} are 1.079 Å, 1.066 Å and 1.019 Å respectively.) [41]. A reasonable first assumption, neglecting relaxation effects, is that Sm^{3+} ions should preferentially occupy the larger octacoordinated Y1 or Y2 sites, leaving the Y3 position fully occupied by Y^{3+} but we shall assess this simple approach later. In order to investigate these possibilities, full-profile Rietveld refinements were carried out. In a first approach, lattice parameters and fractional coordinates of all atoms were

refined, keeping the atomic displacement parameters and occupancy factors fixed. The refined lattice parameters are summarized in Table 1.

Table 1. Refined lattice parameters of $Y_{2-x}Sm_xWO_6$ ($0 \leq x \leq 0.18$) samples.

Compound	*a* (Å)	*b* (Å)	*c* (Å)	*β* (°)	*V* (Å^3)
*Y_2WO_6	7.578(9)	5.330(8)	11.361(18)	104.36(9)	444.61(12)
$Y_{1.98}Sm_{0.02}WO_6$	7.5809(16)	5.3342(12)	11.372(2)	104.334(13)	445.55(17)
$Y_{1.94}Sm_{0.06}WO_6$	7.5838(16)	5.3365(11)	11.376(2)	104.329(13)	446.09(16)
$Y_{1.90}Sm_{0.10}WO_6$	7.5886(17)	5.3389(12)	11.382(3)	104.332(14)	446.78(17)
$Y_{1.86}Sm_{0.14}WO_6$	7.5909(17)	5.3413(12)	11.386(2)	104.317(14)	447.32(17)
$Y_{1.82}Sm_{0.18}WO_6$	7.590(2)	5.3424(14)	11.387(3)	104.312(16)	447.4(2)

*values taken from reference [40]

The smooth increase in the lattice parameters with increasing Sm^{3+} content indicates the formation of a solid solution over the studied composition range. Although Y1 and Y2 have eight neighbouring oxygen atoms, the polyhedral volume of Y2 is marginally larger than that of Y1. Attempts to refine the occupancy factors of Y^{3+}/Sm^{3+} on the three Y sites for the sample $Y_{1.98}Sm_{0.02}WO_6$, resulted in zero occupancy of Sm^{3+} of sites Y2 and Y3, but it did refine well for site Y1. The results for all samples are summarized in Table 2. At low concentrations there is a strong preference of Sm^{3+} for the Y1 position. Interestingly, in samples with 3 – 7% Sm, the dopant ion also sits at the Y3 site. This result seems to be at odds with the small relative volume (17.4 Å) for this site considering it just sevenfold coordinated. If one includes the eighth O atom in an extended 7+1 coordination, the polyhedral volume of the site increases to 22.5 Å^3, a value close to those for the Y1 (21.4 Å^3) and Y2 (22.9 Å^3) sites. Thus occupation of the Y3 sites should not be discarded a priori on steric grounds. Finally, the sample with 9% Sm has all three Y sites more or less equally populated by Sm.

Table 2. Refined Y^{3+}/Sm^{3+} occupancy factors of $Y_{2-x}Sm_xWO_6$ ($0 \leq x \leq 0.18$) samples.

	1% Sm	3% Sm	5% Sm	7% Sm	9% Sm
Y1/Sm1 (2e)	0.94(10)/0.06(10)	0.94(10)/0.06(10)	0.85(11)/0.15(11)	0.82(8)/0.18(8)	0.89(10)/0.11(10)
Y2/Sm2 (2f)	1.01(9)/0.00	1.01(9)/0.00	0.98(9)/0.02(9)	0.99(7)/0.01(7)	0.86(8)/0.14(8)
Y3/Sm3 (4g)	1.05(7)/0.00	0.96(7)/0.04(7)	0.98(7)/0.02(7)	0.92(5)/0.08(5)	0.93(6)/0.07(6)
Refined composition	$Y_{1.958}Sm_{0.042}WO_6$	$Y_{1.932}Sm_{0.068}$	$Y_{1.889}Sm_{0.111}$	$Y_{1.829}Sm_{0.171}$	$Y_{1.805}Sm_{0.195}$
R_p/%	16.75	16.04	18.08	15.40	16.78
R_{wp}/%	26.83	26.13	28.77	25.21	27.45
R_F/%	6.64	6.58	8.06	5.50	5.95

The apparent preference of Sm for the Y1 and Y3 sites at concentrations < 9% of Sm may have implications for the optical properties of this material, since the interatomic distance Y1 – Y3 is the shortest of all the possible Y – Y lengths in this crystal structure (see Table 3) and Y3 – Y3 is only slightly longer. The substitution pattern seems to be somewhat different to similar systems such as Eu^{3+}-doped Y_2WO_6, in which Eu^{3+} seems to occupy Y1 and Y2 sites at low concentrations while at higher concentrations Y3 is gradually also occupied [42] despite the similarity of the ionic radii of Sm^{3+} and Eu^{3+}. In La^{3+}-doped Y_2WO_6, the larger La^{3+} (eightfold 1.16 Å) mainly occupies the Y2 and Y3 sites [43]. Here the occupation of all three sites for the 9% sample, however, indicates that the substitutional energies of Sm into the three different sites are similar and that kinetic effects at the high temperatures where the phases are formed may be more important in determining the occupancies of the different sites than the relative substitution energies. If the substitution pattern is also affected by any tendency of Sm^{3+} ions to group in clusters, as suggested by the spectroscopic evidence below, then the actual site occupation by Sm^{3+} will be highly dependent on a range of factors including concentration and the preparation protocol. Thus the pattern is difficult to predict by simple arguments regarding the relative polyhedral volumes of the different Y sites in undoped Y_2WO_6. This will be addressed further below by first principles electronic structure calculations.

Table 3. Shortest Y-Y interatomic distances *d* under 4 Å and their multiplicity *m* in Y_2WO_6.

Atoms	*m*	*d* / Å
Y1 – Y3	2x	3.6698(21)
Y1 – Y3	2x	3.6761(14)
Y1 – Y2	2x	3.8048(5)
Y1 – Y3	2x	3.9999(22)
Y2 – Y3	2x	3.6992(22)
Y2 – Y3	2x	3.7595(22)
Y3 – Y3	1x	3.7199(11)

3.2 Absorption and optical properties

The measured absorption spectra of $Y_{0.82}Sm_{0.18}WO_6$ in the UV and NIR zones are shown in Figure 2. From these spectra it is possible to assign 19 bands corresponding to the transition from the $^6H_{5/2}$ ground state of Sm to various excited states. In order to obtain the nephelauxetic ratio and the bonding parameter, which is a measure of the expansion of the electron density due to the presence of ligands, here the neighbouring oxygen atoms, the energy levels of the absorption bands of the doped phases were compared with those of the Sm^{3+} aquo ion. [44, 45].

Table 4 shows the energies of the absorption bands of Sm^{3+} in $Y_{0.82}Sm_{0.18}WO_6$, energy assignments for the Sm^{3+} aquo ion, and the nephelauxetic ratio for each energy level. The bonding parameter (δ) is also calculated. According to Sinha [45], the nephelauxetic ratio, β, is given by

$$\beta = \upsilon_d/\upsilon_a \qquad \text{Eq. 1}$$

where υ_d is the frequency for a transition in the doped phase and υ_a is the same transition frequency in the aquo complex. The bonding parameter (δ) is evaluated

using the equation proposed by Thomas et al. [12], where $\delta=100(1-\beta')/\beta'$. Here β' is the average value of the nephelauxetic ratio of the transitions observed in the absorption spectra. The positive value of the bonding parameter (δ) reveals a greater degree of covalency in the Sm-O bonds than in the aquo ion.

Table 4.- Energy level assignments for Sm^{3+} in $Y_{0.82}Sm_{0.18}WO_6$, Sm^{3+}(aquo), nephelauxetic ratios for each transition (β). The average nephelauxetic ratio (β'), and the bonding parameter (δ) are given at the bottom of the table.

$S`L`J`\ {}^6H_{5/2}$	$\nu_c(cm^{-1})$	$\nu_a(cm^{-1})$	β	$S`L`J`\ {}^6H_{5/2} \rightarrow$	$\nu_c(cm^{-1})$	$\nu_a(cm^{-1})$	β
${}^4P_{3/2}$	31447	31550	0.9967	${}^4I_{13/2}$	21413	21600	0.9914
${}^4D_{7/2}$	29155	29100	1.0019	${}^4I_{11/2}$	20408	21100	0.9672
${}^4H_{7/2}$	28653	28250	1.0143	${}^6I_{11/2}$	10593	10500	1.0089
${}^4D_{3/2}$	28011	27700	1.0112	${}^6F_{9/2}$	9276	9200	1.0083
${}^6P_{7/2}$	26455	26750	0.9890	${}^6F_{7/2}$	8097	8000	1.0121
${}^4L_{15/2}$	25575	26650	0.9597	${}^6F_{5/2}$	7246	7100	1.0206
${}^6P_{3/2}$	24570	24950	0.9848	${}^6F_{3/2}$	6748	6630	1.0177
$({}^6P, {}^4P)_{5/2}$	23753	24050	0.9876	${}^6H_{15/2}$	6506		
${}^4G_{9/2}$	22831	22700	1.0058	${}^6F_{1/2}$	6447	6400	1.0074
${}^4F_{5/2}$	22124	22200	0.9966	${}^4I_{13/2}$	21413	21600	0.9914
$\beta` = 0,9990$				$\delta = 0,1046$			

3.3 Diffuse reflectance measurements

The diffuse reflectance spectra of undoped Y_2WO_6 and $Y_{2-x}Sm_xWO_6$ (x=0.02, 0.06, 0.10, 0.14 and 0.18) where the diffuse reflectance has been converted into an absorption using the Kubelka-Munk approximation [46] is shown in Figure 3. These spectra are typical for compounds doped by Ln^{3+} ions, for which the absorption peaks due to f-f transitions appear below the absorption edge of the undoped matrix. The absorption edge energy (E_g) corresponds to the intersection between the base line

along the energy axis and the extrapolated line from the linear portion of the threshold. The *K/S* ratio implies that R_∞ can only be less than 1 if $K \neq 0$ (Eq. 2),

$$F(R_\infty) = \frac{K}{S} = \frac{(R_\infty - 1)^2}{2R_\infty} \quad \text{Eq. 2}$$

The optical band gap (E_g) for undoped Y_2WO_6 is 3.80 eV, which is in good agreement with a previous value reported experimentally [47].The absorption spectra for doped samples show that the Sm 4f electrons are indeed strongly localized and do not significantly affect the magnitude of the band gap when the contents of samarium is changed between x = 0.02 and 0.18. In Sm-doped Y_2WO_6 samples, E_g values vary from 3.40 eV to 3.58 eV with Eg increasing with increasing Sm^{3+} content in the host-structure.

3.4 Luminescence spectra

The excitation spectrum of $Y_{1.94}Sm_{0.06}WO_6$ is shown in the inset of Figure 4. Y_2WO_6 is an optically active matrix involved in the luminescent process. It is a bright photoluminescent material that emits a pale blue light (450 nm) under ultraviolet light excitation [13]. The photo luminescence excitation (PLE) spectra of the Sm-doped Y_2WO_6 samples are dominated by a broad band at about 270 nm consisting mainly of overlapping O^{2-}–Sm^{3+} and O^{2-}–W^{6+} charge transfer bands along with very weak parity forbidden f-f transitions at about 360 nm ($^6H_{9/2} \rightarrow {}^6H_{5/2}$), 380 nm ($^6H_{5/2} \rightarrow {}^4D_{3/2}$), and 410 nm ($^6H_{5/2} \rightarrow {}^4L_{13/2}$).

Room temperature emission spectra of the Sm-doped Y_2WO_6 samples are shown in Figure 4. Intra-configurational 4f-4f transitions of Sm^{3+} were observed. All phases show four main narrow emission lines corresponding to the $^4G_{5/2} \rightarrow 6H_{5/2}$ (c.a. 550-580 nm), $^4G_{5/2} \rightarrow {}^6H_{7/2}$ (c.a. 580-630 nm), $^4G_{5/2} \rightarrow {}^6H_{9/2}$ (c.a. 630-680 nm) and $^4G_{5/2} \rightarrow {}^6H_{11/2}$ (c.a. 680-730 nm) transitions. The most intense emission is observed for $Y_{1.94}Sm_{0.06}WO_6$ with x = 0.03 while at higher doping levels the emission decreases due to concentration quenching. The emission spectra show also a well known broad band at about 450 nm, originating from the WO_6^{6-} groups of the host structure [11]. This emission band vanishes progressively as the concentration of Sm^{3+} is increased.

The chromaticity coordinates (CIE) of the different $Y_{2-x}Sm_xWO_6$ (x=0.00, 0.02, 0.06, 0.10, 0.14 and 0.18) samples under 300 nm excitation were calculated using the Force 2.0 software (see Figure 5) showing that for x ≥ 0.03, the CIE values remain essentially unchanged.

For a good characterization of the photoluminescence properties of Sm^{+3}-doped Y_2WO_6, it is important to determine the critical distance R_o for energy transfer between donors and acceptors, which can be estimated using the equation proposed by Blase et al. [48].

$$R_o = 2\left(\frac{3V}{4\pi\chi_c N}\right)^{1/3} \qquad \text{Eq.3}$$

where V the unit cell volume, χ_c the critical concentration (i.e. the concentration for which emission reaches a maximum), and N the number of formula units in the unit cell. Using V=446.09 $Å^3$, χ_c= 0.03, and N=4, the calculated critical distance is 19.2 Å. This value is much larger than the typical distances for effective exchange interactions (about 4-5 Å). A possible explanation of a critical distance too large for effective exchange interaction is that the energy transfer takes place when the rare-earth cations are clustered together, rather than when randomly distributed in the host structure. We return to investigate the possibility of such clustering in more detail in the theoretical calculations we report later.

In order to evaluate the energy transfer (*ET*) efficiency (η_{ET}) from the host structure to the activator ions, we estimated the emission intensities of the matrix in the presence (I_s) and absence (I_{s0}) of Sm^{3+}. These are calculated using equation 4 [49-51].

$$\eta_{ET} = 1 - \frac{I_s}{I_{s0}} \qquad (4)$$

ET efficiencies were calculated using the spectra measured at 300 nm excitation. As shown in Table 5, the values of η_{ET} increase with increasing Sm^{3+} concentration, whereas the experimental quantum yield (Φ) decreases. The increase in η_{ET} can be explained by the increase of the concentration of activator ions in the host-matrix. On

the other hand, a cross relaxation process could be responsible for the decrease of Φ with increasing Sm^{3+} concentration.

Table 5. ET efficiency and quantum yield (Sm^{3+}) in $Y_{2-x}Sm_xWO_6$ phosphors

Phosphor	η_{ET}	$\Phi_{(Sm3+)}$
$Y_{1.98}Sm_{0.02}WO_6$	41.5	27.3
$Y_{1.94}Sm_{0.06}WO_6$	71.6	23.6
$Y_{1.90}Sm_{0.10}WO_6$	85.8	17.2
$Y_{1.86}Sm_{0.14}WO_6$	86.5	11.1
$Y_{1.82}Sm_{0.18}WO_6$	88.8	10.2

The effect of the concentration of Sm^{3+} on the emission decay curves was also investigated. The results are shown in Figure 6 and reveal that the lifetimes decrease with increasing Sm^{3+}concentration, hinting at cross relaxation of the photoluminescence process.

In order to analyze the decay curves and to obtain more information on the energy transfer, the Hinokuyi-Hirayama model was used [52]. This model assumes that the distribution of the activator ions is random in the host-matrix. The Inokuti-Hirayama equation takes the form:

$$I_t = I_0 \exp\left[-\left(\frac{t}{\tau}\right) - \left(\frac{C}{C_0}\right)\Gamma\left(1-\frac{3}{s}\right)\left(\frac{t}{\tau}\right)^{3/s}\right] \qquad (5)$$

where τ is the intrinsic lifetime of a single ion, *C* is the acceptor concentration, C_0 the critical concentration of acceptors, Γ the gamma function, and *s* a parameter that depends on the type of interaction. The critical concentration C_0 is defined as C_0 =

$3/(4\pi R_0^3)$, where R_0 is the critical transfer distance, the distance between donor and acceptor at which the probability of energy transfer per unit time is equal to the probability of decay of the donor per unit time.

The interaction between the donor and acceptor ions can be described by the energy transfer parameter (Q). The Q value is given by:

$$Q = \frac{4\pi}{3}\Gamma\left(1-\frac{3}{s}\right)C(R_0)^3 \qquad (6)$$

For s=6, the Γ function has the value 1.77 and the interaction is dipole-dipole; for s=8, the Γ function equals 1.43 and the interaction is dipole-quadrupole; when s=10, the Γ function has the value 1.30 and the interaction is quadrupole-quadrupole. The decay curves for all phases $Y_{2-x}Sm_xWO_6$ (x = 0.00, 0.02, 0.06, 0.10, 0.14 and 0.18) were fitted assuming dipole-dipole interaction (Figure 6) and an intrinsic lifetime of τ=1.0 ms.

Figure 7 shows that Q varies linearly with Sm^{3+} concentration. The intercept on the vertical axis in Figure 7 is not equal to zero, which could indicate the Sm^{3+} ions cluster at all compositions, a result in line with the analysis obtained from the calculation of the critical distance. A quite different situation is observed in the Eu-doped phosphors, which follow the Inokuti-Hirayama model [42].

4. Computational results

In order to study the possible preferences for Sm substitution and the possibility of clustering in Y_2WO_6 we have undertaken a series of first principles DFT based calculations for different models of Sm and Eu doped Y_2WO_6 with either 3.125% or 6.25% activator ions.

To check our computational method is able to reproduce accurately the electronic structure of Y_2WO_6 we first optimized the structure of Y_2WO_6 using two different functionals. The calculated lattice parameters for Y_2WO_6 are in good agreement with experiment (Table 6) and with earlier calculations using a somewhat different

computational approach [17]. In our calculations, the HSE06 functional gives a structure that is slightly closer to experiment. The cell parameters calculated with the PBE functional, while also in reasonable agreement, slightly overestimate the cell volume as is common with GGA-type functionals.

Table 6. Calculated and experimental cell unit parameters and band gaps of Y_2WO_6

	Experiment	PBE	HSE06
a (Å)	7.589	7.551 (-0.5%)	7.492 (-1.3%)
b (Å)	5.334	5.443 (2.0%)	5.387 (1.0%)
c (Å)	11.354	11.600 (2.2%)	11.483 (1.1%)
β	104.41	104.96 (0.5%)	104.75 (0.3%)
V (Å^3)	445.15	460.54 (3.5%)	448.19 (0.7%)
Band gap (eV)	3.80	2.24 (-41.1%)	3.86 (1.6%)

Besides the unit cell parameters, it is also important to check the optimized structures by comparing the detailed geometries for each of the three different yttrium coordination environment. We collect together in table 7 the average Y-O distances, the volumes of the coordination polyhedra and the shape measures with respect to three typical coordination polyhedra for octacoordinated metals, i. e., the cube (CU), the square antiprism (SAPR) and the triangular dodecahedron (TDD) as defined in ref. [39]. Note that for coordination site Y3 we have included the eighth O atom at a distance ~3.1 Å in the first 7+1 type coordination sphere.

Agreement with experiment is good and in particular the calculations reproduce the variations across Y1, Y2 and Y3. Coordination volumes are similar for all three sites, with Y1 the smallest. The largest difference between the experimental and optimized structure is a marked difference in the largest Y3-O distance in the 7+1 coordination sphere around Y3. The experimental value is 3.14 Å [40] while the corresponding PBE, PBESol and HSE06 calculated values are much smaller - 2.63 Å, 2.59 Å and 2.64 Å respectively. Results from an earlier calculation [17] with different methodology suggested a smaller discrepancy with a value of 3.14 Å for this distance. We have only been able to find one reported crystal structure for Y_2WO_6 and so hope

our calculations will encourage further experimental study. Overall the calculated structures do not resolve the question of why the Rietveld analysis indicates substitution occurs at Y1 when it is the smallest site.

Table 7. Calculated and experimental coordination geometries for the three different sites for Y in Y_2WO_6

Site		Experiment	PBEsol
Y1	<*Y-O*> (Å)	2.3545	2.3705
	V_Y (Å^3)	21.4	22.1
	S(CU)	2.906	2.147
	S(SAPR)	4.272	6.446
	S(TDD)	2.899	4.820
Y2	<*Y-O*> (Å)	2.3725	2.3642
	V_Y (Å^3)	22.9	23.0
	S(CU)	5.002	4.656
	S(SAPR)	1.717	1.956
	S(TDD)	1.954	1.744
Y3	<*Y-O*> (Å)	2.4063	2.3685
	V_Y (Å^3)	22.5	22.6
	S(CU)	3.657	3.264
	S(SAPR)	6.036	3.329
	S(TDD)	3.938	3.086

The CShM analysis shows the Y1 environment is closest to cubic, with the optimized geometry closer than the experimental. The Y2 site lies between SAPR and TDD. Due to the 7+1 coordination the Y3 coordination is further away from the canonical polyhedra, but nevertheless is closer to cube/tdd than to the antiprism. In the calculated structures, the Y1 and Y3 sites are more regular than in the experimental.

To study doping of Y_2WO_6 with rare earths we used a 144-atom supercell constructed from a 2×2×1 expansion of the primitive cell of Y_2WO_6. We subsequently optimised

different supercells of the same size replacing (i) one yttrium atom with either Sm or Eu at each of the three different crystallographic Y sites, generating $Y_{31}Ln_1W_{16}O_{96}$ (Ln = Sm or Eu). The stoichiometry of this supercell is thus $Y_{1.9375}Ln_{0.0625}WO_6$ or equivalently 3.125% Ln. The shortest distance between the Ln atom in the unit cell and its periodic images in the supercells is approximately 10.7Å, corresponding to twice the primitive unit cell parameter *b*. To study further the possibility of clustering of Ln atoms at higher concentrations, we have used supercells where we replaced two Y atoms either by two Sm or by two Eu, thus generating several $Y_{30}Ln_2W_{16}O_{96}$ structures with stoichiometry $Y_{1.875}Ln_{0.125}WO_6$ (6.25%) Ln. For each supercell, the shortest distances between the Ln atoms before optimisation are listed in table 4. The energies of the doped supercells were minimised with respect to the atomic positions only. Optimisations with fixed unit-cell dimensions strictly give internal energy changes at constant volume; nevertheless, defect energies thus obtained serve also as a good approximation for defect enthalpies at constant pressure [53], as also confirmed here by a set of test calculations.

As shown in table 6, our calculations using the hybrid HSE06 functional agree well with the experimental band gap of bulk Y_2WO_6 (~3.8 eV) while in contrast, it is underestimated by pure DFT (LDA and GGA). Only the HSE06 band structure and DOS are shown in figure 8 since the pure PBE functional does not describe properly the f bands in doped models. In good agreement with previous work [17], the DOS around the Fermi level is mainly composed of O_{2p} states with smaller contributions from Y at the top of the valence band, while W_{5d} states form the bottom of the conduction band. The empty Y_{4d} states lie higher in energy.

Apart from the appearance of the Sm f-states, the PDOS for undoped Y_2WO_6 and for the lowest energy structure of $Y_{1.875}Sm_{0.125}WO_6$ (the 144-atom supercell) are very similar near the Fermi level. In $Y_{1.875}Sm_{0.125}WO_6$ the band gap is determined by the occupied O_{2p} states at the top of the valence band and the unoccupied Sm 4f and W 5d states at the bottom of the conduction band. The HSE06 band gap calculated for $Y_{1.875}Sm_{0.125}WO_6$ is 3.20 eV, smaller than that of Y_2WO_6 itself, in agreement with experiment. This is consistent with the luminescent process observed experimentally, in which a broad, intense band consisting of overlapping O^{2-}—Sm^{3+} and O^{2-}–W^{6+} charge transfer bands is observed. The overlap of the Sm 4f and O 2p bands supports the non-negligible degree of covalency of the Sm-O bonds. The supplementary information plots the DOS also for other arrangements of the two Sm in the supercell.

These are all similar except for variation in the position of the unoccupied f states lying below the conduction band. These are higher in energy when the Y3 position is occupied, and since in the lowest energy supercell both Y2 and Y3 are occupied there are two separate peaks in the DOS below the conduction band in Figure 8c. For comparison the DOS for the lowest energy $Y_{1.875}WEu_{0.125}WO_6$ supercell in Figure 8d shows only one such peak since only the Y3 site is occupied. The luminescence properties will thus vary with the local environment of the lanthanide. Subtle changes in symmetry may lead to large changes in the spectra.

In order to analyse the local effects of the Y -> Ln substitution further we gather together in table 8 the most relevant information for substitution of Y by either Sm or Eu in the 144-atom supercell.

Table 8. Calculated coordination geometries for the three different sites for Y in $Y_{31}Ln_1W_{16}O_{96}$ models for Ln = Y (undoped Y_2WO_6), Sm, or Eu.

Site		Y	Sm	Eu
Y1	<*Y-O*> (Å)	2.3705	2.3967	2.4319
	V_Y (Å^3)	22.1	23.1	24.1
	S(CU)	2.147	2.184	2.310
	S(SAPR)	6.446	5.716	5.943
	S(TDD)	4.820	4.394	4.601
Y2	<*Y-O*> (Å)	2.3642	2.4186	2.4468
	V_Y (Å^3)	23.0	24.7	25.5
	S(CU)	4.656	4.844	4.699
	S(SAPR)	1.956	2.025	2.103
	S(TDD)	1.744	1.584	1.660
Y3	<*Y-O*> (Å)	2.3685	2.4173	2.4551
	V_Y (Å^3)	22.6	24.2	25.4
	S(CU)	3.264	3.457	3.449
	S(SAPR)	3.329	3.144	3.289
	S(TDD)	3.086	2.966	3.027

Table 8 shows that replacement of Y^{3+} by the slightly larger Sm^{3+} or Eu^{3+} leads to an increase, as expected, in the polyhedral volume of about 1-2 $Å^3$ for Sm and 2-3 $Å^3$ for Eu, with the smallest changes at the smaller Y1 site. Consideration of tabulated ionic radii [41] alone would suggest this is counterintuitive since Sm^{3+} has a slightly larger radius than Eu^{3+}. Some resolution of this puzzle is provided by the calculated Mulliken charges on the two dopant atoms. The charges on Sm^{3+} are approximately +2.4*e* while those on Eu^{3+} are considerably lower, approximately 1.4*e*, and while too much significance should not be paid to the absolute values of these charges due to the well-known problems with Mulliken analysis, the difference between the charges suggests that as a dopant here Sm may well be smaller than Eu. It is also interesting to see that the geometry of the coordination site, as indicated by the small changes in the shape measures, is mostly preserved upon substitution, indicating that the effect of replacing Y^{3+} by a larger cation results just in an isotropic expansion of the coordination sphere.

A puzzle which we have been unable to resolve is the disagreement between the occupation of the cationic sites by Sm^{3+} given by the Rietveld analysis and the calculated site energies. For $Y_{1.969}Sm_{0.031}WO_6$, i.e. with one Sm atom in the 144 atom supercell (3.25% Sm), occupation of the Y2 site by Sm is lowest in energy, Y3 substitution is very similar in energy, only 0.041 eV higher, and Y1 much higher, by 0.450 eV. These values agree with the trend in the polyhedral volumes with Y2 the largest and Y1 significantly smaller than the other two. In contrast, according to the Rietveld analysis, at low concentrations the Y2 site remains unoccupied by Sm, while Y1 is favoured. Size effects are clearly complex in these systems as an analogous calculation for Eu suggests occupation of Y3 rather than Y1 and Y2, which are 0.29 and 0.24 eV higher in energy, respectively. Experimental data are scarce, Mossbauer spectroscopy suggests that Eu appears to sit at the Y1 and Y2 sites at low concentrations and all three sites at higher concentrations [54].

Table 9 reveals an even more complex variation of supercell energy with the location of the dopants when two Ln ions are present in the 144-atom supercell (stoichiometry $Y_{1.875}Ln_{0.125}WO_6$). This is reminiscent of similar complex patterns of substitution in garnets [55, 56] which arise due to complicated strain effects across SiO_4 tetrahedra and AlO_6 octahedra.

Table 9. Relative energies (meV) of different pairs of Sm-Sm and Eu-Eu in $Y_{1.875}Sm_{0.125}WO_6$ and $Y_{1.875}Eu_{0.125}WO_6$, respectively, calculated with the PBE functional using a 144-atom supercell. *d* corresponds to experimental distances in the host undoped material.

pairs	*d* / Å	ΔE / meV	
		$Y_{1.88}Sm_{0.12}WO_6$	$Y_{1.88}Eu_{0.12}WO_6$
Y1-Y3	3.670	463	327
Y1-Y3	3.676	457	313
Y2-Y3	3.699	0	118
Y3-Y3	3.720	5	18
Y2-Y3	3.759	67	123
Y1-Y2	3.805	364	398
Y1-Y2	4.000	438	336
Y3-Y3	4.520	100	31
Y1-Y1	5.334	909	615
Y2-Y2	5.334	17	253
Y3-Y3	5.334	101	17
Y2-Y2	6.007	12	197
Y2-Y2	6.601	8	225
Y2-Y2	8.499	13	221
Y3-Y3	8.519	83	0
Y1-Y1	8.734	892	579
Y1-Y3	9.306	493	296

Comparison of the relative energies indicates that in the supercell lowest in energy is that in which the Sm-Sm distance in the unrelaxed structure is 3.699 Å. In the next lowest energy configuration the Sm-Sm distance is 3.720 Å and is just 5 meV higher in energy. Calculated binding energies of pairs of either Sm or Eu relative to the separated dopants are small and negative hinting, despite the limitations of our model,

at the absence of barriers to cluster formation. These results suggest clustering at Y2-Y3 and Y3-Y3 positions separated only by around 3.7 Å offering support for the experimental results shown in figure 7, but both these Sm arrangements are in disagreement with the Rietveld analysis. It is worth noting also that four Sm-Sm pairs with significantly longer Y2-Y2 distances are also relatively low in energy. There are no low energy Sm-Sm pairs involving Y1 positions. For comparison the results for Eu pairs also shown in Table 9 show a greater preference for Y3 occupation relative to Y2 suggesting less marked clustering.

5 Conclusions

We prepared Y_2WO_6 based phosphors doped with different concentrations of Sm^{3+} *via* a classic solid-state reaction at high temperature. The luminescent properties of the resultant compounds were investigated. A broad band consisting of the overlapping O^{2-}–Sm^{3+} and O^{2-}–WO_6^{6+} charge transfer bands dominates the excitation spectrum. The most intense emission corresponds to the $^4G_{5/2} \rightarrow {}^6H_{9/2}$ transition. An emission band centered at about 450 nm originating from the $(WO_6)^{6-}$ groups of the host structure is also observed in the undoped material, which vanishes as the concentration of Sm^{3+} increases.

The measured decay curves are described by the Inokuti–Hirayama model assuming a dipole–dipole interaction. However, the energy transfer parameter (Q) varies linearly with Sm^{3+} concentration, and the intercept is not equal to zero showing that the Sm^{3+} ions form clusters at all compositions.

Results of structural optimisations of Y_2WO_6 using density functional theory and a range of functionals are in general good agreement with experiment although they highlight one potentially important discrepancy – a marked difference in the largest Y3-O distance in the 7+1 coordination sphere at Y3, where the calculated value is approximately 0.5 Å shorter than experiment. We hope this will encourage new crystallographic studies. We have analysed the different coordination environments at the Y1, Y2 and Y3 sites in detail.

We have also carried out calculations on the Sm- and Eu-doped system. These do not resolve why the experimental Rietveld analysis suggests substitution of Y by Sm

occurs at Y1 when it is the smallest site. Calculation indicates Sm favours the Y2 and Y3 sites; there are no low energy Sm-Sm pairs involving Y1 positions. These results suggest clustering at Y2-Y3 and Y3-Y3 positions which are separated only by around 3.7 Å offering support for the experimental photoluminesence results. Size effects are complicated as analogous calculations for Eu suggest a marked preference for Y3 rather than Y1 and Y2. The calculated positive charge on Eu is smaller than that on Sm which will determine its effective size. The greater preference for Y3 also suggests less marked clustering. There are many possible reasons for the differences between the theory and the Rietveld analysis which we hope future work may resolve. In particular the experimental synthesis could be kinetically rather than thermodynamically controlled, and our calculations are all in the static limit and restricted to a small range of dopant concentrations with an artificial periodicity enforced by the supercell.

The calculated band gaps both for the parent compound and the Sm-doped material are in excellent agreement with experiment. There is substantial overlap between the occupied 4f and oxygen 2p bands. The corresponding densities of states show that there is a marked variation in the position of the unoccupied f levels below the conduction band depending on the site occupied by the lanthanide dopant. Thus we expect a difference in the luminesence properties of the Sm- and Eu-doped materials because of the different site occupancies and the relative preference of Eu solely for the Y3 position.

Acknowledgements

This work was supported by FONDECYT, Chile (Grants 1181302, 3170076 and 11171063), the Ministerio de Ciencia, Innovación y Universidades - Spain (Project PGC2018-093863-B-C22), the Maria de Maeztu Units of Excellence Program (MDM-2017-0767), and Generalitat de Catalunya (2017SGR1289). The authors gratefully appreciate the contribution of the Unidad de Equipamiento Científico - MAINI, Universidad Católica del Norte, for supporting sample preparation, analysis and data acquisition by XRD - Proyecto FIC-Regional EQU-25 Conicyt 2009-2010. The computational work made use of the computational facilities of the Advanced Computing Research Centre, University of Bristol—www.bris.ac.uk/acrc/.

REFERENCES

[1] M. Song, W. Zhao, W. Ran, J. Xue, Y. Liu, J.H. Jeong, Multicolor tunable luminescence and energy transfer mechanism in a novel single-phase $KBaGd(WO_4)_3$: Tb^{3+}, Eu^{3+} phosphor for NUV WLEDs, J. Alloys Compd. 803 (2019) 1063-1074.

[2] S. Jaiswal, N. Sawala, P. Nagpure, V. Bhatkar, S. Omanwar, Visible quantum cutting in Tb^{3+} doped $BaGdF_5$ phosphor for plasma display panel, J. Mat. Sci: Materials in Electronics 28 (2017) 2407-2414.

[3] J. Du, O.Q. De Clercq, D. Poelman, Temperature dependent persistent luminescence: Evaluating the optimum working temperature, Sci. Rep. 9 (2019) 10517.

[4] P. Du, Q. Zhang, X. Wang, L. Luo, W. Li, Upconversion luminescence, temperature sensing and internal heating behaviors of Er^{3+}/Yb^{3+}/Fe^{3+}-tridoped $NaBiF_4$ nanoparticles, J. Alloys Compd. 805 (2019) 171-179.

[5] E. Cortés-Adasme, M. Vega, I. Martin, J. Llanos, Synthesis and characterization of $SrSnO_3$ doped with Er^{3+} for up-conversion luminescence temperature sensors, RSC Advances 7 (2017) 46796-46802.

[6] W. Cai, Z. Zhang, Y. Jin, Y. Lv, L. Wang, K. Chen, X. Zhou, Application of TiO_2 hollow microspheres incorporated with up-conversion $NaYF_4$:Yb^{3+}, Er^{3+} nanoparticles and commercial available carbon counter electrodes in dye-sensitized solar cells, Solar Energy 188 (2019) 441-449.

[7] J. Llanos, R. Castillo, D. Espinoza, R. Olivares, I. Brito, Red-emitting $Ln_{2-x}Eu_xTe_2O_6$:RE (Ln=La, Y; RE=Sm^{3+}, Gd^{3+}) phosphors prepared by the Pechini sol–gel method, J. Alloys Compd. 509 (2011) 5295-5299.

[8] F. Meng, H. Zhang, C. Chen, S.I. Kim, H.J. Seo, X. Zhang, A study of luminescence from Eu^{3+}, Ce^{3+}, Tb^{3+} and Ce^{3+}/Tb^{3+} in new potassium gadolinium phosphate $K_3Gd_5(PO_4)_6$, J. Alloys Compd. 671 (2016) 150-156.

[9] H. Marzougui, I. Martin, S. Attia-Essaies, D.B. Hassen-Chehimi, E. Lalla, S. Léon-Luis, Site selective luminescence of Eu^{3+} ions in $K_2Mg(SO_4)_2{\cdot}6H_2O$ crystal, Opt. Mater. 46 (2015) 339-344.

[10] E. Cortés-Adasme, R. Castillo, S. Conejeros, M. Vega, J. Llanos, Behavior of Eu ions in $SrSnO_3$: Optical properties, XPS experiments and DFT calculations, J. Alloys Compd. 771 (2019) 162-168.

[11] Y. Zhou, X. Ge, Z. Zhang, W. Luo, H. Xu, W. Li, J. Zhu, Design and realization on orange-red emitting of samarium activated sodium lanthanum metaphosphate with low CCT and high CP, J. Alloys Compd. 811 (2019) 152020.

[12] S. Thomas, R. George, S.N. Rasool, M. Rathaiah, V. Venkatramu, C. Joseph, N. Unnikrishnan, Optical properties of Sm^{3+} ions in zinc potassium fluorophosphate glasses, Opt. Mater. 36 (2013) 242-250.

[13] H.J. Borchardt, Yttrium-tungsten oxides, Inorg. Chem. 2 (1963) 170-173.

[14] Y. Zhang, B. Ding, L. Yin, J. Xin, R. Zhao, S. Zheng, X. Yan, Monoclinic $Lu_{2-x}Sm_xWO_6$-based white light-emitting phosphors: from ground–excited-states calculation prediction to experiment realization, Inorg. Chem. 57 (2017) 507-518.

[15] J. Llanos, D. Olivares, V. Manríquez, D. Espinoza, I. Brito, Synthesis and luminescent properties of two different Y_2WO_6:Eu^{3+} phosphor phases, J. Alloys Compd. 628 (2015) 352-356.

[16] R. Van Deun, D. Ndagsi, J. Liu, I. Van Driessche, K. Van Hecke, A.M. Kaczmarek, Dopant and excitation wavelength dependent color-tunable white light-emitting Ln^{3+}:Y_2WO_6 materials (Ln^{3+}= Sm, Eu, Tb, Dy), Dalton Trans. 44 (2015) 15022-15030.

[17] P. Alemany, J. Llanos, Electronic, structural, and optical properties of Y_2WO_6, a host material for inorganic phosphors, J. Alloys Compd. 819 (2020) 152958.

[18] V. Petříček, M. Dušek, L. Palatinus, Crystallographic computing system JANA2006: general features, Z. Kristallogr. 229 (2014) 345-352.

[19] D. Wood, J. Tauc, Weak absorption tails in amorphous semiconductors, Phys. Rev. B 5 (1972) 3144.

[20] R. Dovesi, A. Erba, R. Orlando, C.M. Zicovich‐Wilson, B. Civalleri, L. Maschio, M. Rérat, S. Casassa, J. Baima, S. Salustro, Quantum‐mechanical condensed matter simulations with CRYSTAL, Wiley Interdiscip. Rev. Comp. Mol. Sci. (2018) e1360.

[21] See http://www.crystal.unito.it for details on the CRYSTAL code, computational schemes, etc.

[22] R. Dovesi, V. R. Saunders, C. Roetti, R. Orlando, C. M. Zicovich-Wilson, F. Pascale, B. Civalleri, K. Doll, N. M. Harrison, I. J. Bush, P. D'Arco, M. Llunell, M. Causà, Y. Noël, L. Maschio, A. Erba, M. Rerat and S. Casassa CRYSTAL17 User's Manual (University of Torino, Torino, 2017).

[23] J.P. Perdew, K. Burke, M. Ernzerhof, Generalized gradient approximation made simple, Phys. Rev. Lett. 77 (1996) 3865-3868.

[24] J.P. Perdew, A. Ruzsinszky, G.I. Csonka, O.A. Vydrov, G.E. Scuseria, L.A. Constantin, X.L. Zhou, K. Burke, Restoring the density-gradient expansion for exchange in solids and surfaces, Phys. Rev. Lett. 100 (2008) 136406.

[25] J. Heyd, G.E. Scuseria, M. Ernzerhof, Hybrid functionals based on a screened Coulomb potential, J. Chem. Phys. 118 (2003) 8207-8215.

[26] J. Heyd, J.E. Peralta, G.E. Scuseria, R.L. Martin, Energy band gaps and lattice parameters evaluated with the Heyd-Scuseria-Ernzerhof screened hybrid functional, J. Chem. Phys. 123 (2005) 174101.

[27] J. Laun, D. Vilela Oliveira, T. Bredow, Consistent gaussian basis sets of double- and triple-zeta valence with polarization quality of the fifth period for solid-state calculations, J. Comput. Chem. 39 (2018) 1285-1290.

[28] F. Cora, A. Patel, N.M. Harrison, R. Dovesi, C.R.A. Catlow, An ab initio Hartree− Fock study of the cubic and tetragonal phases of bulk tungsten trioxide, J. Am. Chem. Soc. 118 (1996) 12174-12182.

[29] J.K. Desmarais, A. Erba, R. Dovesi, Generalization of the periodic LCAO approach in the CRYSTAL code to g-type orbitals, Theor. Chem. Acc. 137 (2018) 28.

[30] R. Dovesi, R. Orlando, B. Civalleri, C. Roetti, V.R. Saunders, C.M. Zicovich-Wilson, CRYSTAL: a computational tool for the ab initio study of the electronic properties of crystals, Z. Kristallogr. 220 (2005) 571-573.

[31] H.J. Monkhorst, J.D. Pack, Special points for brillouin-zone integrations, Phys. Rev. B 13 (1976) 5188-5192

[32] H. Zabrodsky, S. Peleg, D. Avnir, Continuous symmetry measures, J. Am. Chem. Soc. 114 (1992) 7843-7851.

[33] M. Pinsky, D. Avnir, Continuous symmetry measures. 5. The classical polyhedra, Inorg. Chem. 37 (1998) 5575-5582.

[34] D. Casanova, J. Cirera, M. Llunell, P. Alemany, D. Avnir, S. Alvarez, Minimal distortion pathways in polyhedral rearrangements, J. Am. Chem. Soc. 126 (2004) 1755-1763.

[35] S. Alvarez, D. Avnir, M. Llunell, M. Pinsky, Continuous symmetry maps and shape classification. The case of six-coordinated metal compounds., New J. Chem. 26 (2002) 996-1009.

[36] S. Alvarez, P. Alemany, D. Casanova, J. Cirera, M. Llunell, D. Avnir, Shape maps and polyhedral interconversion paths in transition metal chemistry, Coord. Chem. Rev. 249 (2005) 1693-1708

[37] K.M. Ok, P.S. Halasyamani, D. Casanova, M. Llunell, P. Alemany, S. Alvarez, Distortions in octahedrally coordinated d(0) transition metal oxides: A continuous symmetry measures approach, Chem. Mater. 18 (2006) 3176-3183.

[38] D. Casanova, J.M. Bofill, P. Alemany, S. Alvarez, Shape and symmetry of heptacoordinate transition-metal complexes: structural trends, Chem. Eur. J. 9 (2003) 1281-1295.

[39] D. Casanova, M. Llunell, P. Alemany, S. Alvarez, The rich stereochemistry of eight-vertex polyhedra: a continuous shape measures study, Chem. Eur. J. 11 (2005) 1479-1494.

[40] V. Efremov, A. Tyulin, V. Trunov, O. Kudin, V. Yanovskij, V. Voronkova, Crystal structure of monoclinic Y_2WO_6 and Yb_2WO_6, Kristallografiya 28 (1984) 904-909.

[41] R.D. Shannon, Revised effective ionic radii and systematic studies of interatomic distances in halides and chalcogenides, Acta Crystallogr. - Sect. A Cryst. Phys. Diffr. Theor. Gen. Crystallogr. 32 (1976) 751-767.

[42] J. Llanos, D. Espinoza, R. Castillo, Energy transfer in single phase Eu^{3+}-doped Y_2WO_6 phosphors, RSC Advances 7 (2017) 14974-14980.

[43] B. Ding, C. Han, L. Zheng, J. Zhang, R. Wang, Z. Tang, Tuning oxygen vacancy photoluminescence in monoclinic Y_2WO_6 by selectively occupying yttrium sites using lanthanum, Sci. Rep. 5 (2015) 9443.

[44] W. Carnall, P. Fields, K. Rajnak, Electronic energy levels in the trivalent lanthanide aquo ions. I. Pr^{3+}, Nd^{3+}, Pm^{3+}, Sm^{3+}, Dy^{3+}, Ho^{3+}, Er^{3+}, and Tm^{3+}, J. Chem. Phys. 49 (1968) 4424-4442.

[45] S.P. Sinha, Complexes of the Rare Earths, Pergamon Press, Oxford (1966).

[46] W.W. Wendlandt, H.G. Hecht, Reflectance spectroscopy, Interscience, New York, 1966.

[47] B. Ding, H. Qian, C. Han, J. Zhang, S.-E. Lindquist, B. Wei, Z. Tang, Oxygen vacancy effect on photoluminescence properties of self-activated yttrium tungstate, J. Phys. Chem. C 118 (2014) 25633-25642.

[48] G. Blasse, Energy transfer in oxidic phosphors, Philips Res. Rep. 24 (1969) 131.

[49] U. Caldino, J. Hernández-Pozos, C. Flores, A. Speghini, M. Bettinelli, Photoluminescence of Ce^{3+} and Mn^{2+} in zinc metaphosphate glasses, J. Phys.: Condens. Matter 17 (2005) 7297-7305.

[50] U. Caldino, A. Speghini, M. Bettinelli, Optical spectroscopy of zinc metaphosphate glasses activated by Ce^{3+} and Tb^{3+} ions, J. Phys.: Condens. Matter 18 (2006) 3499-3508.

[51] G. Ju, Y. Hu, L. Chen, X. Wang, Z. Mu, H. Wu, F. Kang, Luminescence properties of Y_2O_3: Bi^{3+}, Ln^{3+} (Ln= Sm, Eu, Dy, Er, Ho) and the sensitization of Ln^{3+} by Bi^{3+}, J. Lumin. 132 (2012) 1853-1859.

[52] M. Inokuti, F. Hirayama, Influence of energy transfer by the exchange mechanism on donor luminescence, J. Chem. Phys. 43 (1965) 1978-1989.

[53] M. Taylor, G. Barrera, N.L. Allan, T. Barron, W. Mackrodt, Free energy of formation of defects in polar solids, Faraday Discuss. 106 (1997) 377-387.

[54] H. Van Noort, T. Popma, Concentration-dependent site occupancy in europium-doped Y_2WO_6 as studied by ^{151}Eu Mössbauer spectroscopy, Solid State Commun. 55 (1985) 77-79.

[55] C.L. Freeman, N.L. Allan, W. van Westrenen, Local cation environments in the pyrope–grossular $Mg_3Al_2Si_3O_{12}$–$Ca_3Al_2Si_3O_{12}$ garnet solid solution, Phys. Rev. B 74 (2006) 134203.

[56] C.L. Freeman, M.Y. Lavrentiev, N.L. Allan, J.A. Purton, W. van Westrenen, Similarity in silicate chemistry: trace elements in garnet solid solutions, J. Mol. Struct. THEOCHEM 727 (2005) 199-204.

Figure captions

Figure 1. Crystal structure of the monoclinic phase Y_2WO_6 (left) and coordination polyhedra of Y atoms (right).

Figure 2. Absorption spectrum of $Y_{0.82}Sm_{0.18}WO_6$. UV region (left) and NIR region (right).

Figure 3. Diffuse reflectance spectra of $Y_{2-x}Sm_xWO_6$ (x=0.02, 0.06, 0.10, 0.14 and 0.18) after a Kubelka-Munk transformation.

Figure 4. Emission spectra of $Y_{2-x}Sm_xWO_6$ (x=0.02, 0.06, 0.10, 0.14 and 0.18) (λ_{ex}=300 nm). The inset shows the excitation spectrum of $Y_{0.82}Sm_{0.18}$ WO_6 (λ_{em}=612 nm).

Figure 5. CIE chromaticity diagram for $Y_{2-x}Sm_xWO_6$ (x =0.00, 0.02, 0.06, 0.10, 0.14 and 0.18) phosphors.

Figure 6. Sm^{3+} concentration dependence of the decay curves of $Y_{2-x}Sm_xWO_6$ (λ_{ex}=300 nm, λ_{ex}=612 nm).

Figure 7. Q vs concentration of Sm^{3+}in $Y_{2-x}Sm_xWO_6$ phosphors.

Figure 8. (a) Band structure and (b) Density of States (DOS) for Y_2WO_6, (c) Density of States (DOS) for the lowest energy 144-supercells of stoichiometry $Y_{1.875}WSm_{0.125}WO_6$ and (d) $Y_{1.875}WEu_{0.125}WO_6$. Note that in the Sm supercell both Y2 and Y3 sites are occupied, while Eu is located only at the Y3 site.

Figure 1.

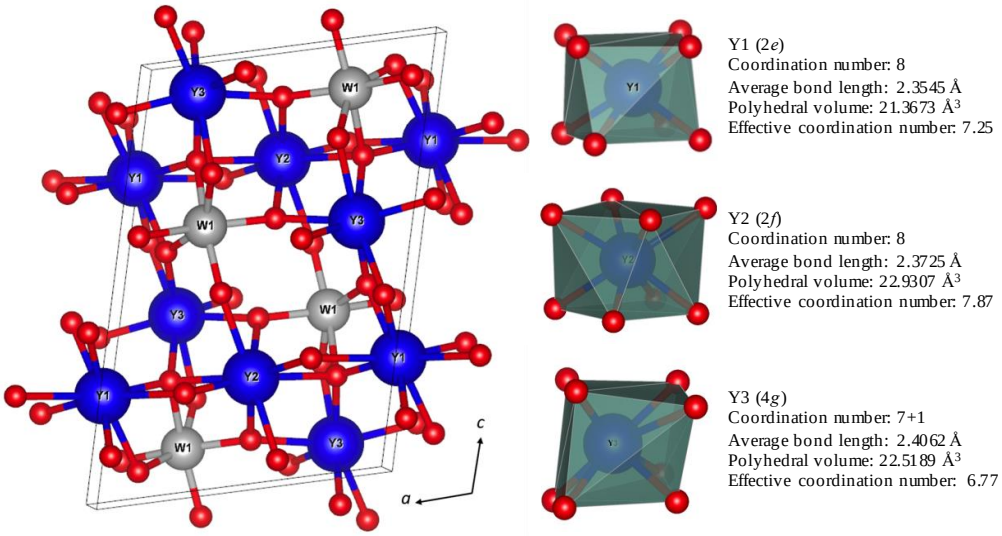

Y1 (2*e*)
Coordination number: 8
Average bond length: 2.3545 Å
Polyhedral volume: 21.3673 Å^3
Effective coordination number: 7.25

Y2 (2*f*)
Coordination number: 8
Average bond length: 2.3725 Å
Polyhedral volume: 22.9307 Å^3
Effective coordination number: 7.87

Y3 (4*g*)
Coordination number: 7+1
Average bond length: 2.4062 Å
Polyhedral volume: 22.5189 Å^3
Effective coordination number: 6.77

Figure 2.

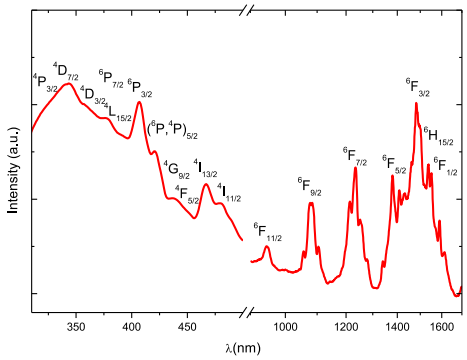
Intensity (a.u.)
λ(nm)
350
400
450
1000
1200
1400
1600
$^4P_{3/2}$
$^4D_{7/2}$
$^6P_{7/2}$
$^6P_{3/2}$
$^4D_{3/2}$
$^4L_{15/2}$
$(^6P,^4P)_{5/2}$
$^4G_{9/2}$
$^4I_{13/2}$
$^4F_{5/2}$
$^4I_{11/2}$
$^6F_{11/2}$
$^6F_{9/2}$
$^6F_{7/2}$
$^6F_{5/2}$
$^6F_{3/2}$
$^6H_{15/2}$
$^6F_{1/2}$

Figure 3.

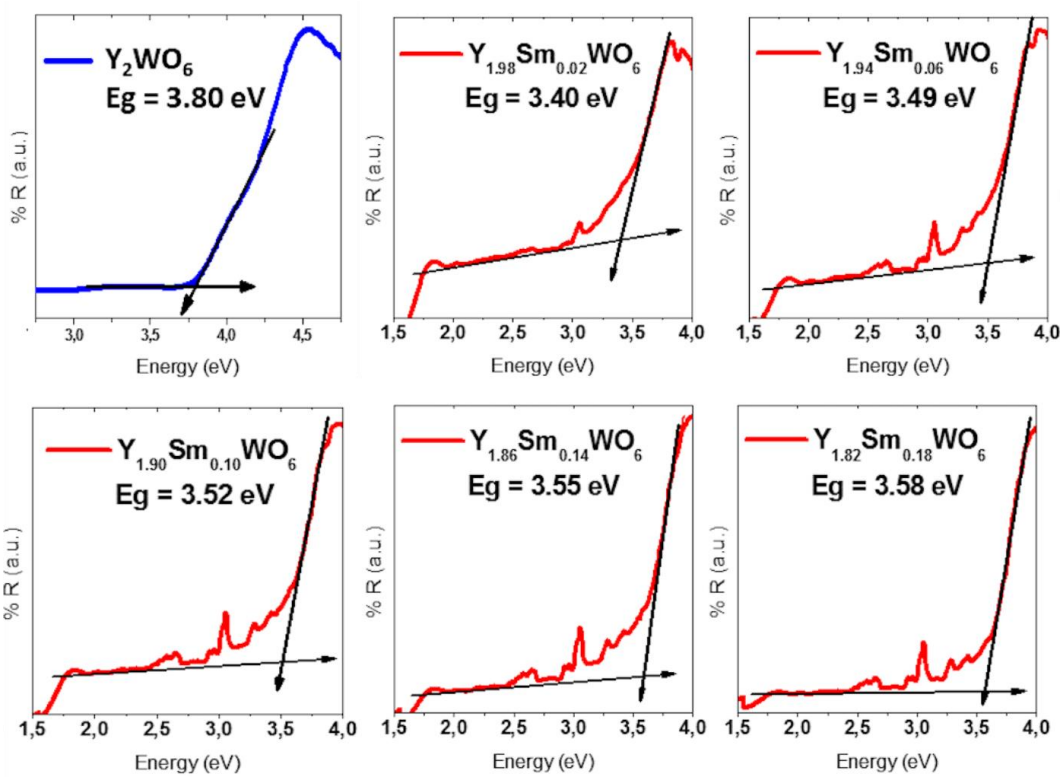
Y2WO6
Eg = 3.80 eV
Y1.98Sm0.02WO6
Eg = 3.40 eV
Y1.94Sm0.06WO6
Eg = 3.49 eV
Y1.90Sm0.10WO6
Eg = 3.52 eV
Y1.86Sm0.14WO6
Eg = 3.55 eV
Y1.82Sm0.18WO6
Eg = 3.58 eV
% R (a.u.)
Energy (eV)

Figure 4.

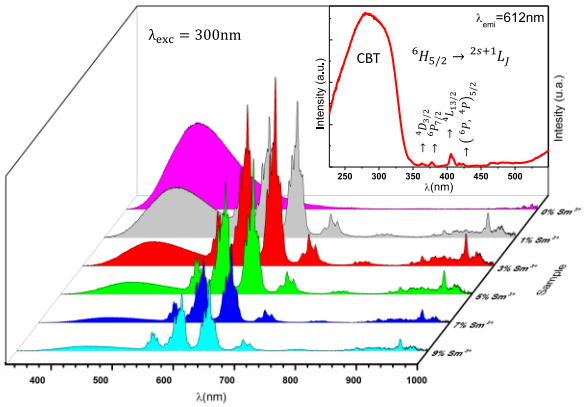
λexc = 300nm
λemi=612nm
CBT
$^6H_{5/2} \rightarrow {}^{2s+1}L_J$
Intensity (a.u.)
Intesity (u.a.)
λ(nm)
0% Sm3+
1% Sm3+
3% Sm3+
5% Sm3+
7% Sm3+
9% Sm3+
Samples
400
500
600
700
800
900
1000

Figure 5.

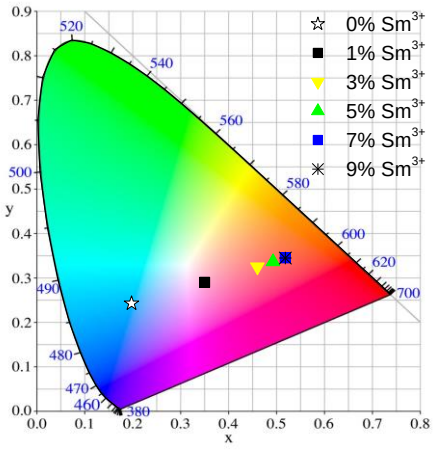

Figure 6.

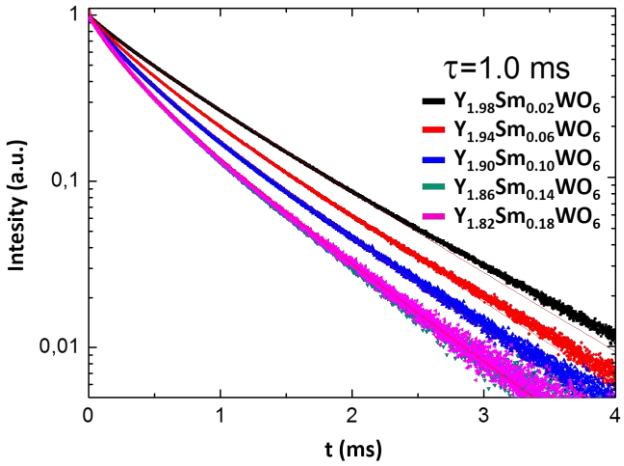
τ=1.0 ms
$Y_{1.98}Sm_{0.02}WO_6$
$Y_{1.94}Sm_{0.06}WO_6$
$Y_{1.90}Sm_{0.10}WO_6$
$Y_{1.86}Sm_{0.14}WO_6$
$Y_{1.82}Sm_{0.18}WO_6$
Intesity (a.u.)
1
0,1
0,01
0
1
2
3
4
t (ms)

Figure 7.

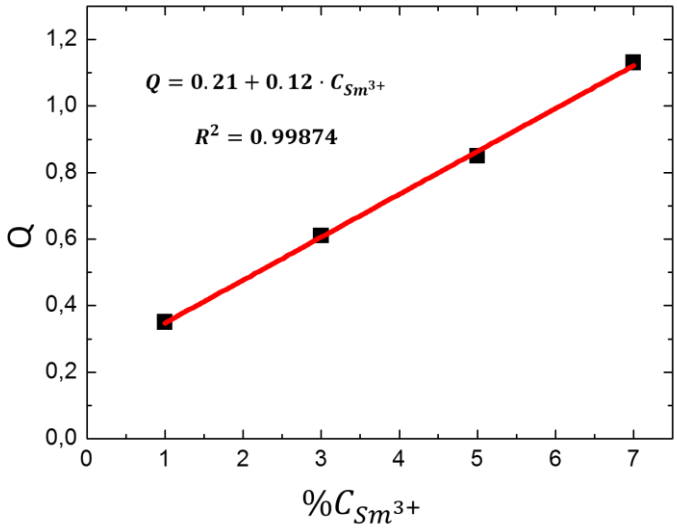
$Q = 0.21 + 0.12 \cdot C_{Sm^{3+}}$
$R^2 = 0.99874$
Q
$\%C_{Sm^{3+}}$
0,0
0,2
0,4
0,6
0,8
1,0
1,2
0
1
2
3
4
5
6
7

Figure 8.

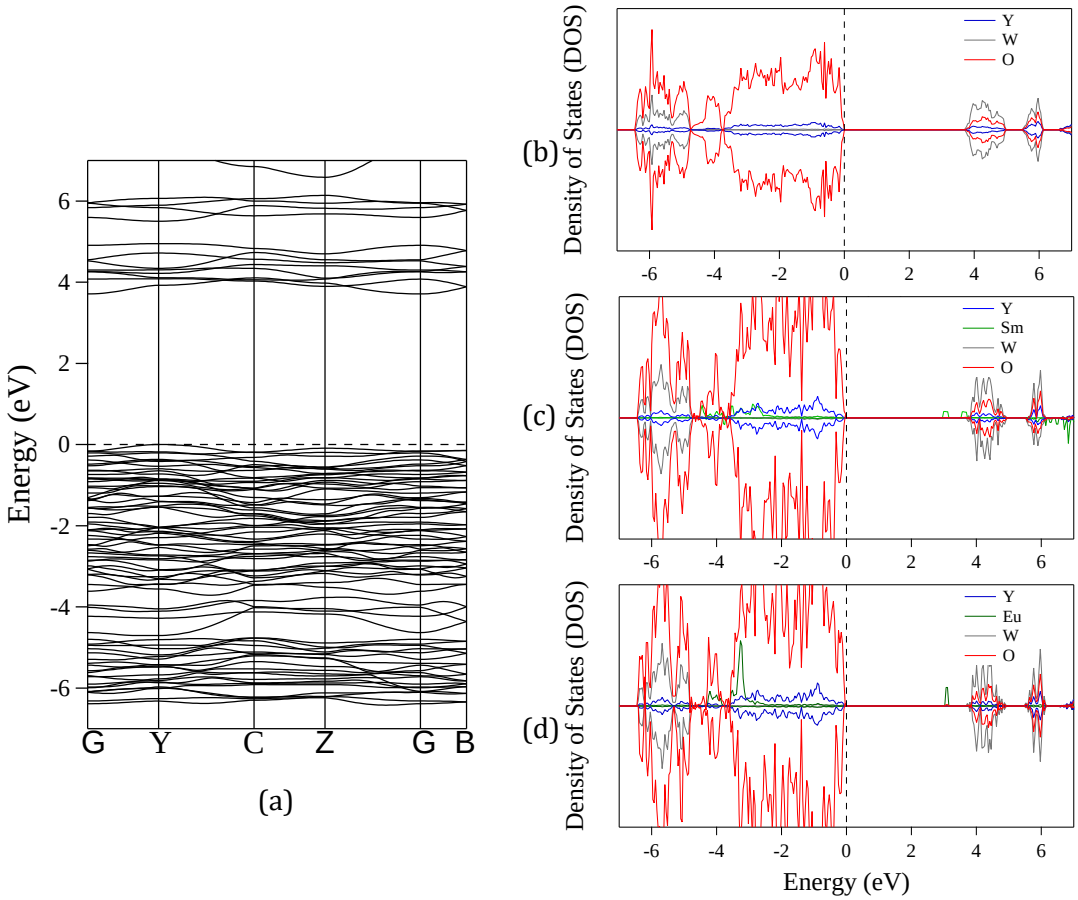
Energy (eV)
6
4
2
0
-2
-4
-6
G
Y
C
Z
G
B
(a)
(b)
Density of States (DOS)
Y
W
O
(c)
Density of States (DOS)
Y
Sm
W
O
(d)
Density of States (DOS)
Y
Eu
W
O
-6
-4
-2
0
2
4
6
Energy (eV)